Bioactive Materials 17 (2022) 147–161

Contents lists available at ScienceDirect

Bioactive Materials

journal homepage: www.keaipublishing.com/en/journals/bioactive-materials

CXCR4-guided liposomes regulating hypoxic and immunosuppressive microenvironment for sorafenib-resistant tumor treatment

Yuehua Wang [a,b,1], Zhenjie Wang [c,1], Fei Jia [d], Qing Xu [b], Zhilin Shu [b], Junlin Deng [b], Aimin Li [a,***], Meng Yu [b,**], Zhiqiang Yu [a,b,*]

[a] Cancer Center, Integrated Hospital of Traditional Chinese Medicine, Southern Medical University. Guangzhou, 510315, PR China
[b] Guangdong Provincial Key Laboratory of New Drug Screening, School of Pharmaceutical Sciences, Southern Medical University, Guangzhou, 510515, PR China
[c] The People's Hospital of Gaozhou, Maoming, 525200, PR China
[d] CAS Key Laboratory of Standardization and Measurement for Nanotechnology, CAS Key Laboratory for Biomedical Effects of Nanomaterials and Nanosafety, CAS Center for Excellence in Nanoscience, National Center for Nanoscience and Technology of China, Beijing, 100190, PR China

ARTICLE INFO

Keywords:
Hepatocellular carcinoma
Sorafenib resistance
Hypoxia relief
Immunotherapy
Tumor targeting regulation

ABSTRACT

Clinical sorafenib treatment could activate C-X-C receptor type 4 (CXCR4)/stromal source factor-1α (SDF-1α) axis to aggravate intra-tumoral hypoxia of hepatocellular carcinoma (HCC), which further leads to progression, invasion, metastasis, and immunosuppression of tumors and in return causes resistance to sorafenib therapy. Therefore, a multi-functional oxygen delivery nanoplatform was rationally constructed based on an oxygen-saturated perfluorohexane (PFH)-cored liposome, with the CXCR4 antagonist LFC131 peptides modifying on the surface to simultaneously deliver sorafenib and the CSF1/CSF1R inhibitor PLX3397 (named PFH@LSLP) for sorafenib-resistant HCC treatment. The PFH@LSLP was developed to overcome sorafenib resistance by synergistic effects of the following 3 roles: 1) the O_2-saturated PFH core could alleviate the tumor hypoxia by O_2 supply; 2) the LFC131 peptide recognized the hypoxia-related overexpressed CXCR4 and then blocked SDF-1α/CXCR4 axis to re-sensitize the HCC cells to sorafenib; 3) PLX3397 activated the immune responses via inhibiting the CSF1/CSF1R pathway in TAMs, further enhanced $CD8^+$ T cell infiltration to reverse immunosuppression in tumors. Antitumor performance on H22 tumor-bearing mice and HCC patient-derived tumor xenograft (PDX) model showed that PFH@LSLP could overcome sorafenib resistance by synergistic effect of hypoxia attenuation, resistance-related gene regulation, and immune-microenvironment modification.

Hepatocellular carcinoma (HCC) is one of the leading causes of cancer-related death worldwide [1,2]. Because only a few patients of developing HCC are qualified for surgical removal or transplantation, what's more the exceptional resistance to chemotherapy further hinders HCC therapy [3,4]. HCC is a hypervascular tumor with abundant blood vessel abnormalities, thus causes hypoxic circumstance especially in deep tumor tissue, which is the main cause of failure of solid tumor treatment [5–7]. As a clinical first-line drug, sorafenib is a multi-kinase inhibitor that displays a significant role in advanced HCC treatment by blocking tumor angiogenesis and inhibiting HCC cell proliferation [8,9]. Unexpectedly, sorafenib exhibits limited cytotoxicity to distal tumors because of the poor penetration and intra-tumoral hypoxia-induced resistance [10]. Tumor hypoxia can induce cell cycle arrest, increase protein resistance, and lead to drug resistance and ineffective treatment [11,12]. In recent years, a variety of strategies have been attempted to improve therapeutic efficiency by alleviating tumor hypoxia [13]. Representatively, O_2-carrying nanomaterials were explored to directly supply O_2 to hypoxic microenvironment to improve oxygen-dependent therapeutical efficiency [14]. Amongst, a clinical artificial blood substitute, perfluorohexane (PFH) has been extensively used owing to its high affinity to O_2 and good biocompatibility to deliver O_2 to overcome hypoxia-related drug resistance [15,16].

Peer review under responsibility of KeAi Communications Co., Ltd.
* Corresponding author. Cancer Center, Integrated Hospital of Traditional Chinese Medicine, Southern Medical University. Guangzhou, 510315, PR China.
** Corresponding author.
*** Corresponding author.
E-mail addresses: liaimin2005@163.com (A. Li), yumeng999@smu.edu.cn (M. Yu), yuzq@smu.edu.cn (Z. Yu).
[1] Yuehua Wang and Zhenjie Wang contributed equally to this work.

https://doi.org/10.1016/j.bioactmat.2022.01.003
Received 21 October 2021; Received in revised form 31 December 2021; Accepted 2 January 2022
Available online 20 January 2022

However, O_2-carrying PFH encapsulated in nanocarriers only could attenuate hypoxia in some extent, many antitumor therapeutics limited by hypoxic conditions themselves could lead to deterioration of hypoxia by persistently consuming O_2 or upregulating expression of hypoxia-related proteins during the treating process, e.g. sorafenib, photodynamic therapy, and radiotherapy. There is evidence that the sorafenib could activate C-X-C receptor type 4 (CXCR4)/stromal source factor-1α (SDF-1α) axis to induce aggravated intra-tumoral hypoxia of HCC, which further leads to progression, invasion, and metastasis of tumors and resistance to anti-angiogenic therapy [17–19]. To focus this drug resistance pathway, LFC131, a CXCR4 antagonist, was designed to recognize and bind to the overexpressed CXCR4 on sorafenib-resistant HCC cell surface, thus enhancing cytotoxicity by regulating Akt/ERK/p38 MAPK/caspase signaling pathways [20,21]. Moreover, LFC131 peptides sensitized HCC to sorafenib by blocking SDF-1α/CXCR4 axis that induced cancer cell proliferation and tumor-promoting microenvironment polarization [22,23]. Therefore, we rationally speculated that LFC131 (CXCR4 inhibitors) would perform synergically antitumor effect with sorafenib *via* targeting tumor cells and then inhibit their SDF-1α/CXCR4 axis, meanwhile regulating hypoxic microenvironment to suppress sorafenib resistance.

In addition to hypoxic conditions, increasing evidence indicate that the insufficient efficacy of sorafenib treatment is also closely related to the adaptive mechanisms of tumor evasion from immune surveillance [24,25], including the expansion of oncogenic TAMs [26], and the intrinsic expression of osteopontin (OPN) or programmed death ligand-1 (PD-L1) on HCC cells [27,28]. Studies have indicated that OPN facilitated chemotactic migration and M2-like polarization of TAMs by activating the colony-stimulating factor 1 (CSF1)/CSF1 receptor (CSF1R) pathway in macrophages, which further resulted to the increase of immunosuppressive cytokines and blocking of antitumor immune responses [29,30]. Previous researchers have used CSF1 inhibitor in HCC therapy to regulate CSF1R expression, thus impeded TAMs recruitment, regulated M2 phenotype polarization and improved the efficacy of immune checkpoint blockade therapy [31,32]. Monoclonal antibodies or small molecule inhibitors targeting the CSF1/CSF1R signaling axis are being used in clinical trials but have some limited efficacy due to poor response rates [33]. It has been reported that the obtained compound PLX3397 is a competitive and highly specific inhibitor of CSF1R tyrosine kinase, which played a critical role in the paracrine interaction between CSF1 and CSF1R in preclinical models [34]. Therefore, it would be a potential therapeutic strategy to combine the CSF1/CSF1R pathway and CXCR4 inhibitors to overcome hypoxic and immunosuppressive conditions in sorafenib-resistant HCC.

In this work, an HCC-specific multidrug delivery liposomal system was developed to overcome sorafenib resistance by synergistic effects of hypoxia attenuation, regulation of resistance-related genes, and reversion of immunosuppressive condition. As shown in Scheme 1, a PFH-cored liposome with the CXCR4 antagonist LFC131 peptides modified on the surface co-delivered sorafenib and the inhibitor PLX3397 (named PFH@LSLP) for sorafenib-resistant HCC treatment. Firstly, the obtained PFH@LSLP specifically bound to CXCR4 overexpressed HCC cells *via* LFC131 and released O_2 into circumstances to overcome hypoxia-related sorafenib resistance. Subsequently, the bound LFC131 significantly blocked the up-regulation and activation of SDF-1α/CXCR4 axis during the process of sorafenib treatment. Further, the loaded PLX3397 was released to remodel tumor immune-microenvironment by blocking the CSF1/CSF1R pathway to reduce M2 phenotypic polarization, which consequently resulted to activation of $CD8^+$ T cells and induction of intracellular immune responses. As a result, prominent antitumor effect could be achieved by synergistic chemotherapy and tumor microenvironment regulation in sorafenib-resistant HCC.

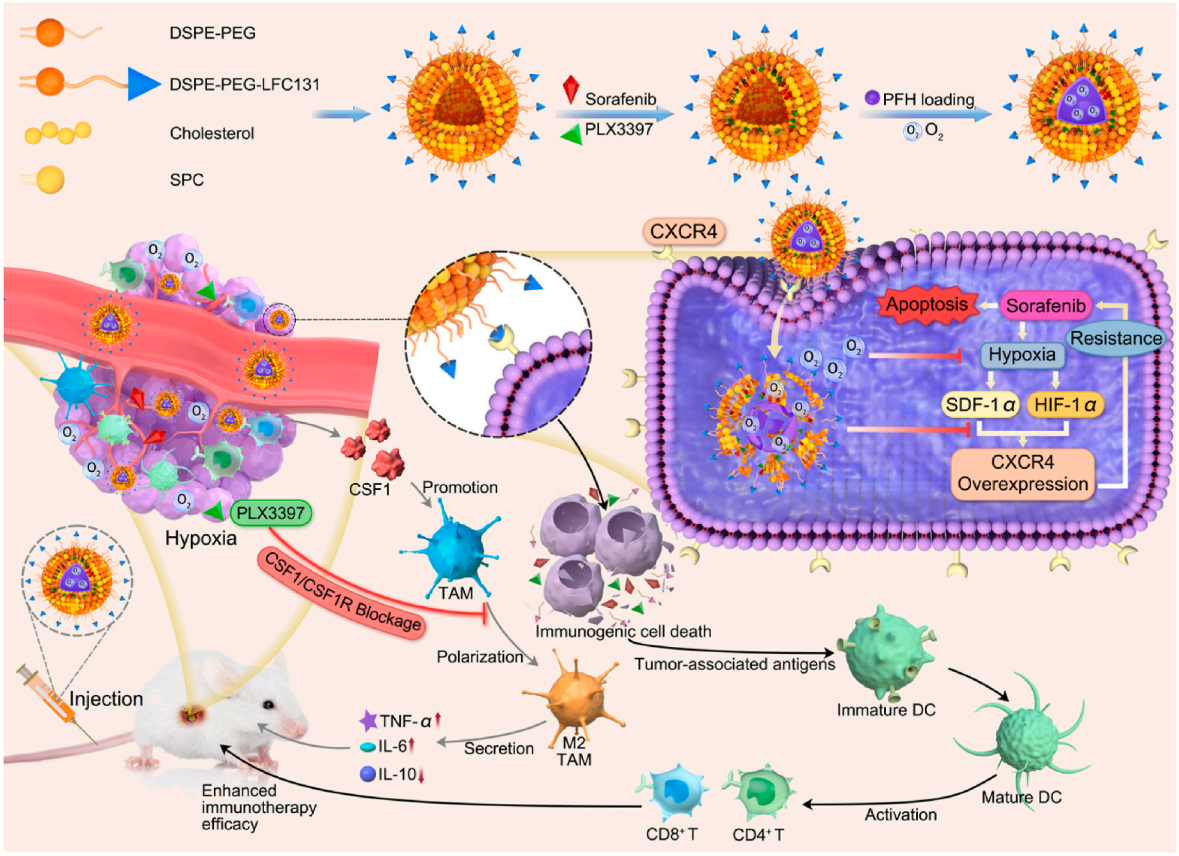

Scheme 1. Schematic illustration of PFH@LSLP-mediated antitumor synergistic therapy by regulating hypoxic and immunosuppressive microenvironment for sorafenib-resistant tumor treatment.

1. Materials and methods

Reagents and Materials. LFC131 peptide (Tyr-Arg-Arg-Nal-Gly, MW 747.82) was synthesized and characterized by Taopu Co. Ltd. (Shanghai, China). Cholesterol (Chol) was purchased from Advanced Vehicle Technology (Shanghai, China). Lecithin (PC) and 1,2-Distearoyl-sn-glycero- 3-phosphoethanolamine-N-[methoxy(poly(ethylene glycol))- 2000] (DSPE-PEG2000) were purchased from RVT Pharmaceutical Technology Co. Ltd. (Shanghai, China). Phosphatidyl ethanolamine (PE) was supplied by Shanghai Fan Ke Biotechnology Co. Ltd. (Shanghai, China). PFH was purchased from Energy Chemical Co. Ltd. (Shanghai, China). Sorafenib (>99%) was obtained from Aladdin Reagent Company (Shanghai, China). All reagents used in this work were of analytical grade without further purification.

Preparation of PFH-encapsulated/Sorafenib and LFC131 Peptide-loaded NPs. To prepare functional nanoparticles, an 50:25:25:5 M ratio of PC:PE:Chol:DSPE-PEG2000 (a total of 30 mg) and LFC131 peptide (0.2 mg/mL) were dissolved in 10 mL chloroform. The solvent was removed by rotary evaporation at 50 °C to form a lipid membrane. Next, 5 mL cold ultra-pure water was added to peel off the membrane for hydration at 45 °C for 5 min. Sorafenib (10 mg/mL, DMF) 50 μL and CSF1 immunosuppressant PLX3397 (0.2 mg/ml in DMSO) are added slowly on ice with an ultrasonic probe. Then, 0.2 mL PFH was added slowly under sonication in an ice bath to form PFH-encapsulated/LFC131 peptide-loaded liposome (4% PFH). PFH@O_2 NPs could be obtained by bubbling O_2 gas with an oxygen cylinder in PFH@NPs solution for 3 min. For the preparation of control-NPs, the liposomes loading Sorafenib (LS) were without PFH addition procedure. Subsequently, NPs were purified by ultrafiltration (3500 MWCO, Millipore Corporation, Bedford, MA) to remove un-encapsulated drugs. NPs were collected at 4 °C for storage.

The characterization of liposomes. The morphology, size distribution, Zeta potential and polydispersity index (PDI) of NPs were determined by transmission electron microscopy (TEM; H-7500, Hitachi High-Tech, Tokyo, Japan) and dynamic light scattering using a Malvern Zetasizer (Nano ZS, Worcestershire, UK) at room temperature.

Drug Loading Capacity (DLC) and Drug Encapsulation Efficiency (DEE) of NPs. The concentration of sorafenib encapsulated in different types of NPs was determined by the HPLC method at 267 nm. LFC131-modified drug-loaded or drug-loaded NPs were dissolved and disintegrated in methanol to completely release the encapsulated drugs. The standard curve for drugs content calculation was obtained by detecting the absorbance of predetermined concentrations of sorafenib at 267 nm. DLC (%) and DEE (%) were analyzed according to the formula below:

$$\text{DLC}\ (\%) = \frac{\text{weight of loaded drug}}{\text{weight of whole NPs}} \times 100$$

$$\text{DEE}\ (\%) = \frac{\text{weight of loaded drug}}{\text{weight of fed drug initially}} \times 100$$

***In Vitro* Drug Release of NPs.** The *in vitro* drug release from NPs was investigated by the dialysis method. Dialysis bags (3.5 kDa molecular weight cut-off; Biotechnology Co., Ltd., China) containing different NPs solution (2 mL) were immersed in 30 ml of PBS (0.01 M, pH 7.4), with vibrating at 100 rpm at 37 °C in a constant temperature incubator shaker (Zhicheng Inc., Shanghai, China). At predetermined time intervals (0, 1, 2, 4, 6, 8, 10,12, 24, 36, 48, 72 h), 0.5 mL of release solution was taken for measurement and replaced with the same volume of fresh medium. The released drugs (Rhodamine B, 200 μL, 10 mg/mL) were determined by the UV-spectrophotometric method (490 nm) as described above.

Measurement of O_2 Release from PFH@LSLP. The O_2 loading and O_2 release of the oxygenated PFH-encapsulated NPs were studied. 1 mL solution of each formulation (PFH@LSLP, PFH@LSP, PFH@LS and LS) was added into 10 mL water pre-deoxygenated via N_2 bubbling. Then, an external ultrasonic agitation (SONICS, power level 130 W, 40 kHz) was applied for 240 s. Then, the dissolved O_2 concentration of the solution was monitored using portable dissolved oxygen meter equipment.

Cell Culture of Liver Cells. HCC cell lines HepG2 (Human) and H22 cells (Mouse) were maintained in Dulbecco's modified Eagle's medium (DMEM) supplemented with 10% (v/v) fetal bovine serum (FBS), 100 U/mL penicillin and 100 μg/mL streptomycin (all purchased from Hyclone Laboratories, Inc., Logan, UT, USA) at 37 °C in a humidified 5% CO_2 incubator.

***In Vitro* Cytotoxicity Assay.** The effect of drugs on cell proliferation was examined by MTT assay. HepG2 cells were incubated in 96-well culture plates ($5*10^3$ cells/well) for 12 h to adhere, the attached cells were taken into a hypoxic box for 6 h. Then the cells were conducted using PFH@LSLP, PFH@LSL, PFH@LS and LS which treated with indicated concentrations of sorafenib drugs (0, 0.5, 2, 4, 8, 20 μM) for 24 h in hypoxic condition, respectively. HepG2 cells in normal culture were used as controls. After 24 h incubation, the cells were incubated with 10 μL MTT (5 mg/mL, Genview, Gen-view scientific Inc., USA) solution at 37 °C for another 4 h, and formazan crystals were dissolved in 150 μL dimethyl sulfoxide (DMSO). Finally, the absorbance was measured at 490 nm using a microplate reader (Tecan, Hombrechtikon, Switzerland). Cell viability was expressed as: Cell viability (%) = $(OD_{sample} - OD_{blank})/(OD_{control} - OD_{blank}) \times 100$.

***In Vitro* Cellular Uptake.** To evaluate the cellular uptake, HepG2 cells were seeded in a 6-well plate ($1 * 10^6$ cells per well), then HepG2 cells were incubated with PFH@LSLP, PFH@LSL, PFH@LS, and LS liposomes with the same concentration of sorafenib (20 μg) in hypoxia condition for 6 h. Since the sorafenib-loaded liposomes are not fluorescent, the Rhodamine B (RhoB) probe was physically loaded in both liposomes. The probe content was quantified using the standard fluorescent approach. Later, the cells were washed with PBS twice, fixed with 4% paraformaldehyde (PFA) for 15 min and stained with DAPI (10 mg/mL) for 15 min. The fluorescence intensity of RhoB (excitation: 488 nm; emission: 515–545) was collected accordingly and quantified by using a confocal microscope (LSM-780, Carl Zeiss, Germany).

For FCM analysis, HepG2 cells were seeded into a 6-well plate. When reached 80% confluence, the cells were given the same treatment, as mentioned in the CLSM observation experiment. After incubation under hypoxia conditions, these cells were washed with PBS three times before digestion using trypsin. The cell suspension was centrifuged at 3000 rpm, 5 min at 4 °C, and resuspended in 0.3 mL of PBS. The cells were analyzed using a BD FACS flow cytometer. The excitation and emission wavelengths were 488 nm and 515–545 nm, respectively.

Apoptosis Assay. The liposomes-induced apoptosis was detected using an Annexin V-FITC/PI Apoptosis Detection Kit (Genview) according to the manufacturer's instructions. Briefly, after incubation with 1.2 mL liposomes (200 μL nanoparticle solution diluted in 1 mL DMEM medium) indicated concentrations of drugs at hypoxia condition for 8 h, the cells (5×10^4) were digested with 0.25% trypsin without EDTA, harvested with low-speed centrifugation, washed with PBS, and incubated with 5 μL Annexin V-FITC and 10 μL PI in 400 μL binding buffer for 10 min in the dark at room temperature. The stained cells were analyzed using a BD FACS flow cytometer (BD Biosciences).

Western Blot Analysis. Western blot was used to detect the effect of liposomes on protein expression. Briefly, after incubation with liposomes indicated concentrations of drugs at hypoxia condition for 24 h, the cells were lysed in RIPA lysis buffer on ice for 30 min. The total proteins were separated using SDS-PAGE and then transferred to PVDF membranes (Bio-Rad, Hercules, CA). First, the membranes were sealed with 10 mL 5% skim milk for 2 h, then, the membranes were incubated with anti-CXCR4 (1:1000, abcam), anti-HIF1α (1:1000), anti-p53 (1:1000) and anti-GAPDH(1:1000, abcam) primary antibodies at 4 °C overnight, respectively. After this incubation, the membranes were washed with PBST three times for 10 min each, and the membranes were incubated with HRP-conjugated secondary antibodies (Beyotime Biotechnology) for 2 h. Finally, the immunoreactive bands were visualized using an Efficient Chemiluminescence Kit (Genview) and

photographed under a ChemiDoc XRS System (Bio-Rad). GAPDH was used as a loading control for western blotting.

H22 and PDX Animal Model of Liver Tumor. All animal studies were performed in accordance with animal protocol procedures of Southern Medical University approved by the Institutional Animal Care and Use Committee (IACUC). All animals were monitored for abnormal behaviors to minimize animal pain and suffering. Female BALB/c mice and BALB/c nude mice aging 5–6 weeks were purchased from Guangdong Medical Laboratory Animal Center. To develop tumors in BALB/c mice, $1 * 10^7$ H22 cells suspended in 100 mL of PBS were subcutaneously implanted in the lateral thigh of mice, and the tumor sizes were monitored every three days. The tumor size of each mice was allowed to grow to 50 mm^3 calculated by: Tumor volume $= 0.5 \times (\text{tumor width})^2 \times (\text{tumor length})$. For PDX HCC-bearing mice model, tumors were exfoliated from subcutaneous HCC-bearing mice first. Then, the tumor tissues were washed with PBS and cut into small pieces (1 mm × 1 mm × 3 mm size), and the pieces were filled into the inoculation needle. The PDX HCC-bearing mouse model was established after two weeks.

***In Vivo* Tumor Imaging.** For *in vivo* fluorescence imaging, mice bearing H22 tumors were intravenously injected with 200 μL PFH@LSLP NPs. Then, fluorescence imaging experiments were performed by Cy5.5 dye on an imaging system (Carestream IS 4000, USA) at 0 h, 4 h, 8 h, 12 h, and 24 h post-injection. Sorafenib-loaded liposomes without PFH, PFH@LSL, and PFH@LS were used as negative controls. After 24 h, the tumor tissues and organs including heart, spleen, lung, kidney, and liver were collected and the fluorescence intensity was analyzed to characterize drug distribution.

***In Vivo* Therapeutic Effects Evaluation.** The therapeutic efficacy of different formulations was investigated in tumor-bearing mice which were established as described above. When the tumor volumes reached about 100 mm^3, the BALB/c mice (n = 6 per group) and nude mice (n = 5 per group) were randomly assigned into five groups, respectively. The mice of each group were administrated intravenously every other day for continuous 7 times with the different formulations as described in the following: (a) PBS, (b) 200 μL LS (sorafenib 1 mg/kg), (c) 200 μl PFH@LS (sorafenib 1 mg/kg), (d) 200 μl PFH@LSL (LFC131-modified sorafenib-loaded NPs, sorafenib 1 mg/kg), (e) 200 μl PFH@LSLP (PLX3397 and LFC131-modified sorafenib-loaded NPs, sorafenib 1 mg/kg). The weight of the mice and the size of the tumors were monitored every other day, and tumor volumes were calculated according to the following formula: Tumor volume $= 0.5 \times (\text{length}) \times (\text{width})^2$. After two days at the end of treatment, the mice were euthanized. The tumor tissues and other organs were excised, washed with PBS, weighed and photographed. Store the tumors at −80 °C for subsequent use.

FCM for tumors. Tumors and lymphocytes from therapeutic experiments of the mentioned mice were used for the analysis and evaluation of immune cells. The infiltrating lymphocytes in tumors (TILs) and lymphocytes of each group were analyzed by FCM (BD FACS, USA). The collected TILs and lymphocytes were incubated with anti–CD45-FITC (BD), anti–CD3-APC-Cy7 (BD), anti–CD8-APC (BD) and anti-CD4-PE-Cy7 (Tonbo) antibodies to determine the content of $CD8^+$ T cells and $CD4^+$ T cells. In addition, the macrophages in the tumor of each group were stained by anti-F4/80-BV421, anti-CD206 (M2), anti-CD86-PE (Biolegend) antibodies (M1). The Tregs infiltrating in the tumors were stained by anti-CD45-FITC, anti–CD25-APC (Tonbo), anti–CD4-PE-Cy7, and anti–Foxp3-PE (BD) antibodies. The ratio of matured DCs in the lymph nodes was also analyzed by FCM after staining with anti–CD11c-violetFluor (Tonbo), anti–CD80-FITC (Biolegend), and anti–CD86-PE (Biolegend) antibodies.

***In Vivo* Therapeutic Mechanisms of PFH@LSLP by RNA Sequencing.** RNA-sequencing performs high-throughput sequencing on the total RNA of different samples, screens differentially expressed genes, and performs Gene Ontology (GO)/Kyoto Encyclopedia of Genes and Genomes (KEGG) enrichment analysis to obtain the biological process and pathway differences between different samples. We performed RNA-sequencing on H22 cells exposed to various treatments to determine the possible cytotoxic mechanisms involved. By RNA sequencing, tumor gene expression profiles of five groups were revealed, including PBS, LS, PFH@LS, PFH@LSL, and PFH@LSLP. Herein, LS, PFH@LS, PFH@LSL and PFH@LSLP were considered as treatment groups, compared with the control group (PBS). Each group had three independent replicates.

Firstly, raw data (raw reads) of fastq format were firstly processed through in-house Perl scripts. Reference genome and gene model annotation files were downloaded from the genome website directly. Then, the Index of the reference genome was built using Hisat2 v2.1.0 and paired-end clean reads were aligned to the reference genome using Hisat2 v2.1.0. Moreover, feature Counts v1.5.0-p3 was used to count the reads numbers mapped to each gene. And then FPKM of each gene was calculated based on the length of the gene and reads count mapped to this gene. Differential expression analysis of two conditions/groups (three biological replicates per condition) was performed using the DESeq2 R package (1.16.1). DESeq2 provides statistical routines for determining differential expression in digital gene expression data using a model based on the negative binomial distribution. Genes with an adjusted P-value <0.05 found by DESeq2 were assigned as differentially expressed.

Gene Ontology (GO) enrichment analysis of differentially expressed genes was implemented by the cluster Profiler R package, in which gene length bias was corrected. GO terms with corrected Pvalue less than 0.05 were considered significantly enriched by differential expressed genes. KEGG is a database resource for understanding high-level functions and utilities of the biological system, such as the cell, the organism and the ecosystem, from molecular-level information, especially large-scale molecular datasets generated by genome sequencing and other high-throughput experimental technologies (http://www.genome.jp/kegg/). We used cluster Profiler R package to test the statistical enrichment of differential expression genes in KEGG pathways.

Tumor immunofluorescence staining and hematological tests. After the treatment, mice bearing H22 tumors and PDX tumors were sacrificed at 24 h after i.v. injection of PFH@LSLP or other NPs, with their tumor tissues harvested, weighed, and repeatedly washed with PBS. These tumor tissues were fixed using 4% paraformaldehyde. The slices of tumor and organs were stained with TUNEL, as well as hematoxylin and eosin staining (H&E) to evaluate the therapeutic effect and systemic toxicity. In addition, for the hypoxia study, rabbit polyclonal anti–HIF–1α (Hypoxia Inducible Factor-1) and anti-CXCR4 antibody as the primary antibody was used for the staining, which was specific indicators help evaluate oxygenation levels. Representative micrographs were collected using a fluorescence microscope (IX71, Olympus).

Blood samples collected from the eyeballs and stored in ethylenediaminetetraacetic acid (EDTA)-coated tubes were employed for the hematological assay. Potential cytotoxic were reflected by the levels of biomarkers, including alkaline phosphatase (ALP), alanine aminotransferase (ALT), aspartate aminotransferase (AST), urea nitrogen (BUN), creatinine (CRE), and globulin (GLB), were determined using an automated biochemical analyzer (Trilogy, France).

Statistics. All statistical analyses were performed by GraphPad Prism 5.0 software. All the quantitative data were described using the mean SD (standard deviations), and statistical analysis was performed with Student's *t*-test and one-way ANOVA followed by a post hoc test. Values of $P < 0.05$ was considered statistically significant ($^*p < 0.05$).

2. Results and discussions

2.1. Design and characterization of HCC-specific PFH@LSLP

Firstly, LFC131 peptide was designed to specifically bind to CXCR4 that overexpressed on sorafenib-resistant HCC cells. The successful synthesis of the LFC131 peptide was evidenced by mass spectrometry (MS) and high-performance liquid chromatography (HPLC) (Figs. S1–S2). Then, LFC131 was decorated on the surface of liposomes

that co-loading with chemotherapeutic drug sorafenib and CSF-1 inhibitor PLX3397 to achieve HCC-specific PFH@LSLP. Fig. 1A has shown the uniform and spherical morphology of liposomes with different drug loading and decorations investigated by transmission electron microscopy (TEM). The hydrodynamic diameter of LS, PFH@LS, PFH@LSL, and PFH@LSLP determined by dynamic light scattering (DLS) was 103.6 nm, 108.2 nm, 114.4 nm and 120.6 nm, respectively (Fig. 1B). Besides, the zeta potentials have shown that all of the liposomes were negatively charged, which contributed to excellent stability and long circulation before reaching tumor tissues. The sorafenib was quantified by HPLC for evaluation of drug loading capacity and cumulative release behaviors. The encapsulation efficiency of sorafenib was determined by HPLC (Fig. S3), which were calculated according to regression equations.

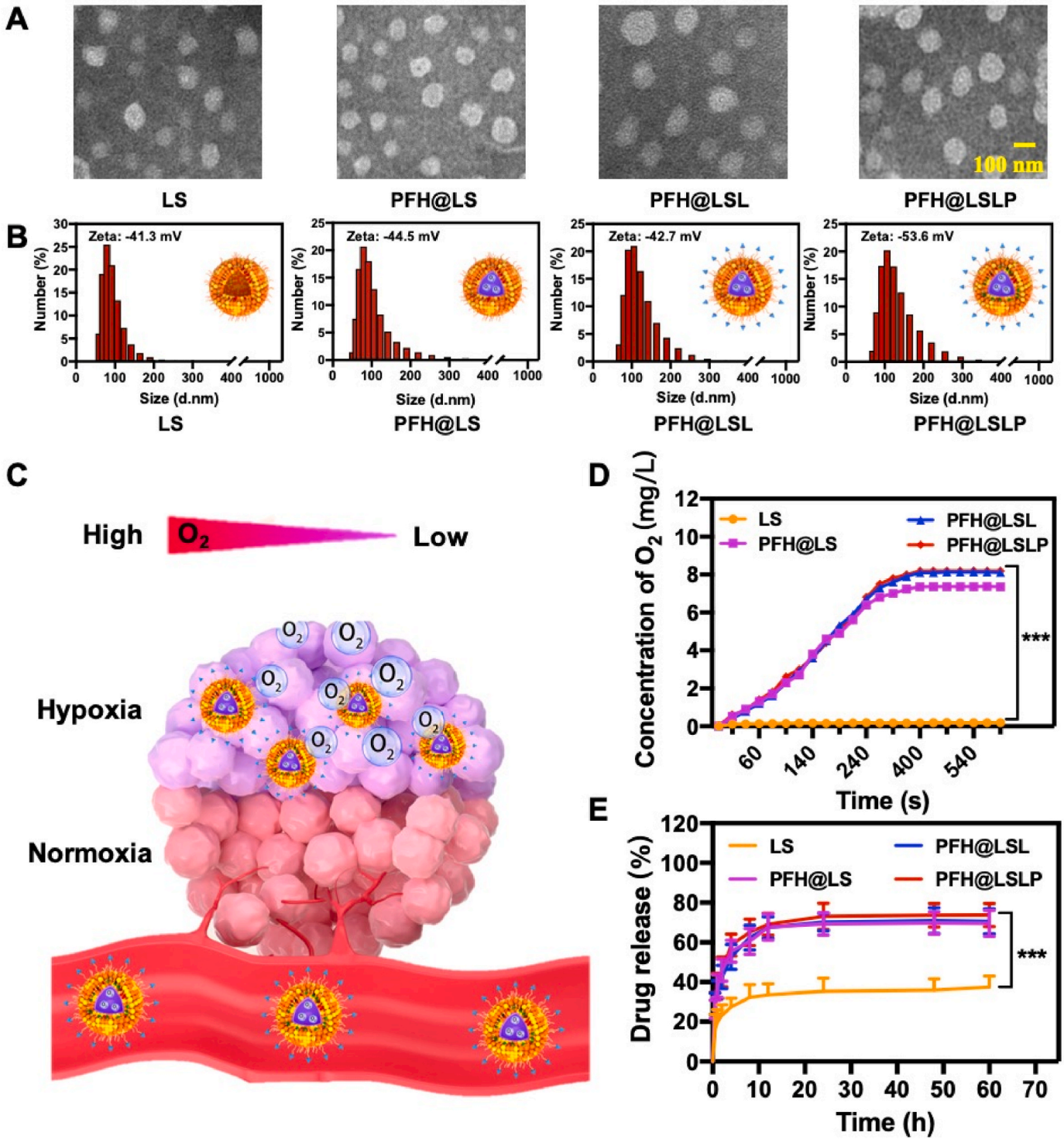

Fig. 1. Characterization of PFH@LSLP NPs. (A) TEM images of LS, PFH@LS, PFH@LSL, and PFH@LSLP. Scale bar: 100 nm. (B) Form diagram and size distribution of different nanoparticles measured by DLS. (C) Schematic illustration of the drug release behavior of PFH@LSLP nanoparticles under hypoxic and normoxic conditions, respectively. (D) The oxygen supply in O_2-deficient solutions containing various nanoparticles. (E) *In vitro* release of sorafenib in hypoxic conditions from LS, PFH@LS, PFH@LSL, and PFH@LSLP. Data are presented as the mean ± SD (n = 3). ***p < 0.001.

Considering that PFH@LSLP was designed to overcome sorafenib-resistance HCC by targeting delivering of O_2 and drugs in hypoxic deep tumor tissue (Fig. 1C), we have evaluated the O_2 supply and sorafenib release properties under hypoxic conditions. Solutions containing different nanoparticles (LS, PFH@LS, PFH@LSL, and PFH@LSLP) were saturated by O_2 and were added into deoxygenated (nitrogen filled) water, which was used to mimic hypoxic conditions in deep tumor, then the change of oxygen concentration in hypoxia environments was monitored using a portable dissolved oxygen meter. As shown in Fig. 1D, the PFH-containing solutions (PFH@LS, PFH@LSL, and PFH@LSLP) rapidly increased the dissolved oxygen concentration up to ~8 mg/L within several minutes compared to that of LS, attributed to their prominent oxygen-carrying capability in presence of PFH and the free diffusion of oxygen *via* concentration gradient under hypoxic environment. The oxygen release from liposomes might destroy the integrity of nanocarriers, which would be conducive to accompanied release of loaded sorafenib (Fig. 1E). Further, the cumulative release behaviors of sorafenib from sorafenib-loaded liposomes were recorded at hypoxic condition by HPLC. The results showed that PFH@LSLP performed a sorafenib release over 70% within 24 h, which was much faster than the ~30% of LS. In a word, the oxygen-saturated PFH containing nanoparticles would alleviate the hypoxic environment by consistently diffuse oxygen and consequently performed a sustained release of carried cargos for therapeutics.

2.2. *In vitro cytotoxicity and hypoxia reversion by PFH@LSLP in hypoxic conditions*

To investigate the *in vitro* cytotoxicity and hypoxia reversion effect of PFH@LSLP in hypoxic conditions, a closed container with an AnaeroPack-Anaero cassette inside was used in order to create hypoxic condition (Fig. 2A). The cells were then cultured with PFH@LSLP and other evaluated nanoparticles in this device and submitted to the biological detections. PFH@LSLP showed a sorafenib concentration-dependent toxicity to HepG2 cells at both hypoxic and normoxic conditions (Fig. 2B), indicating that PFH@LSLP could selectively bind to and kill tumor cells *via* the tumor-specific affinity of LFC131 peptide. It is noteworthy that the differentiation of cytotoxicities among different liposomes under normoxic conditions was not that significant as under hypoxic conditions, because the hypoxia-related signals could cause the resistance to sorafenib via various pathways. The existence of oxygen reservoir PFH (PFH@LS) contributed to a slight improvement of cytotoxicity compared to solely treatment with sorafenib (LS) (Fig. 2B). Meanwhile, the additional presence of LFC131 (PFH@LSL and PFH@LSLP), which was used as a CXCR4 antagonist could further intervene the SDF-1α/CXCR4 signaling pathway to overcome sorafenib-resistance for greater tumor cell killing effects under hypoxic conditions. The cell apoptotic and necrotic proportion of PFH@LSLP was further determined by Flow cytometry (FCM) using Annexin V-FITC/propidium iodide (PI) double staining assay. As shown in Fig. 2C, the percentage of apoptotic and necrosis region after incubation with PFH@LSLP was up to 83.2%, which was much higher than that of LS (3.1%) and PFH@LS (53.4%) treated cells in normoxic conditions. On the contrary, a remarkably higher apoptosis was induced by PFH@LSLP under hypoxic conditions compared with other untargeted liposomes groups. In accordance with the MTT data, PFH@LSLP treatment caused the ratio of apoptotic and necrotic about 58.6%, the apoptosis-inducing capacity of PFH@LSLP suffered slight compromise in hypoxic compared with normoxic conditions, confirming that the CXCR4 targeted-liposomes could improve oxygen dissolution to alleviate hypoxic environment, inhibit tumor cell proliferation and induce cell apoptosis in hypoxic conditions.

Inspired by the *in vitro* antitumor efficacy of PFH@LSLP in hypoxic conditions, we have explored its working mechanism within HepG2 tumor cells. Hypoxia-related signals that caused sorafenib-resistance have been evaluated by combinational application of sorafenib and hypoxia reversion ingredients (Fig. 2D). After treatment with LS-Hypoxia group or PBS-Hypoxia group (simulation of hypoxia conditions induced by sorafenib), the expression of HIF-1α and CXCR4 in HepG2 cells was significantly upregulated compared to PBS-Normoxia group by western bolt and its quantitative analysis (Fig. 2E and Fig. S4). However, PFH@LSL-Hypoxia group and PFH@LSLP-Hypoxia group performed an excellent role on inhibition of SDF-1α/CXCR4 pathway while PFH@LS-Hypoxia group only showed limited effect because of absence of targeting peptide modification. The HIF-1α fluorescence signals in HepG2 cells treated with different solutions were showed the similar trend in consistent with western blotting data (Fig. 2F), further evidenced that sorafenib could cause chemo-resistance through aggravating hypoxia-related signals. Quantified fluorescence intensity of total HIF-1α in HepG2 cells after different treatments was shown in Fig. S5. The results indicated that the tumor cell-specific PFH@LSLP could overcome sorafenib-resistance through alleviating hypoxia by oxygen-saturated PFH while blocking CXCR4 transmembrane protein and the downstream HIF-1α/CXCR4 pathway by LFC131.

2.3. *In vitro and in vivo tumor-specific transportation of PFH@LSLP*

LFC131 was labeled with fluorescein isothiocyanate (FITC) and then was decorated on the surface of PFH@LSLP to track the liposomes. Rho B (200 μL, 10 mg/mL) was directly loaded into the liposomes to mimic the drugs delivered by nanoparticles. After incubation for 4 h at 37 °C, the strongest fluorescence signal observed by confocal laser scanning microscopy (CLSM) and the corresponding highest mean fluorescence intensity (MFI) of Rho B and FITC from PFH@LSLP was observed in the cytosol of HepG2 cells (Fig. 3A and Fig. S6). The results demonstrated the LFC131-mediated highly specific drug delivery capability of PFH@LSLP to tumor cells. The intracellular fluorescence intensity of Rho B was further detected by FCM in Fig. 3B. The much higher intracellular accumulation of Rho B was observed in HepG2 cells cultured with PFH@LSLP and PFH@LSL than that of PFH@LS and LS, which was consistent with the CLSM images.

The tumor-specificity of PFH@LSLP was monitored using IVIS system in H22 tumor-bearing mice. The fluorescence of Cy5.5 (5 mg/mL) loaded in liposomes was used to indicate *in vivo* biodistribution of liposomes. As shown in Fig. 3C and Fig. S7, PFH@LSLP and PFH@LSL showed remarkable tumor accumulative fluorescence signals than other organs and reached peak at 12 h. The *ex vivo* fluorescence images of tumors and major organs (heart, liver, spleen, lung, and kidney) from mice sacrificed 24 h after administration further verified that the LFC131-modified nanoparticles could retention in tumors over 24 h, which facilitated the sustained antitumor effect in tumor tissues (Fig. 3D–E).

2.4. *In vivo antitumor efficacy and biosafety*

The *in vivo* antitumor efficacy was next evaluated on H22 ($1 * 10^6$) tumor-bearing model. The tumors of the mice within 10 days, the H22 tumor-bearing BABL/c mice were randomly divided into 5 groups when the tumors grew to ~100 mm^3 ($n = 6$), and then were intravenously injected with different solutions (PFH@LSLP, PFH@LSL, PFH@LS, LS, and PBS) every two days (Fig. 4A). As shown in Fig. 4B–F, the solely treatment by sorafenib (LS) showed no significant tumor inhibition due to the resistance to sorafenib. In the presence of oxygen reservoir PFH or LFC131, PFH@LS and PFH@LSL performed obvious tumor-suppression, which could be deduced as the roles of hypoxia relief to overcome sorafenib-resistance by supplying oxygen and blocking hypoxia-related pathways. Under the additional function of PLX3397 that reducing macrophage recruitment and predominating in M2 phenotypic polarization *via* blocking the CSF1/CSF1R pathway, PFH@LSLP exhibited the most significant tumor growth inhibition. Meanwhile, no significant body weight loss was found in all treatment groups, reflected the good biocompatibility of the treatments (Fig. 4E). Additionally, the

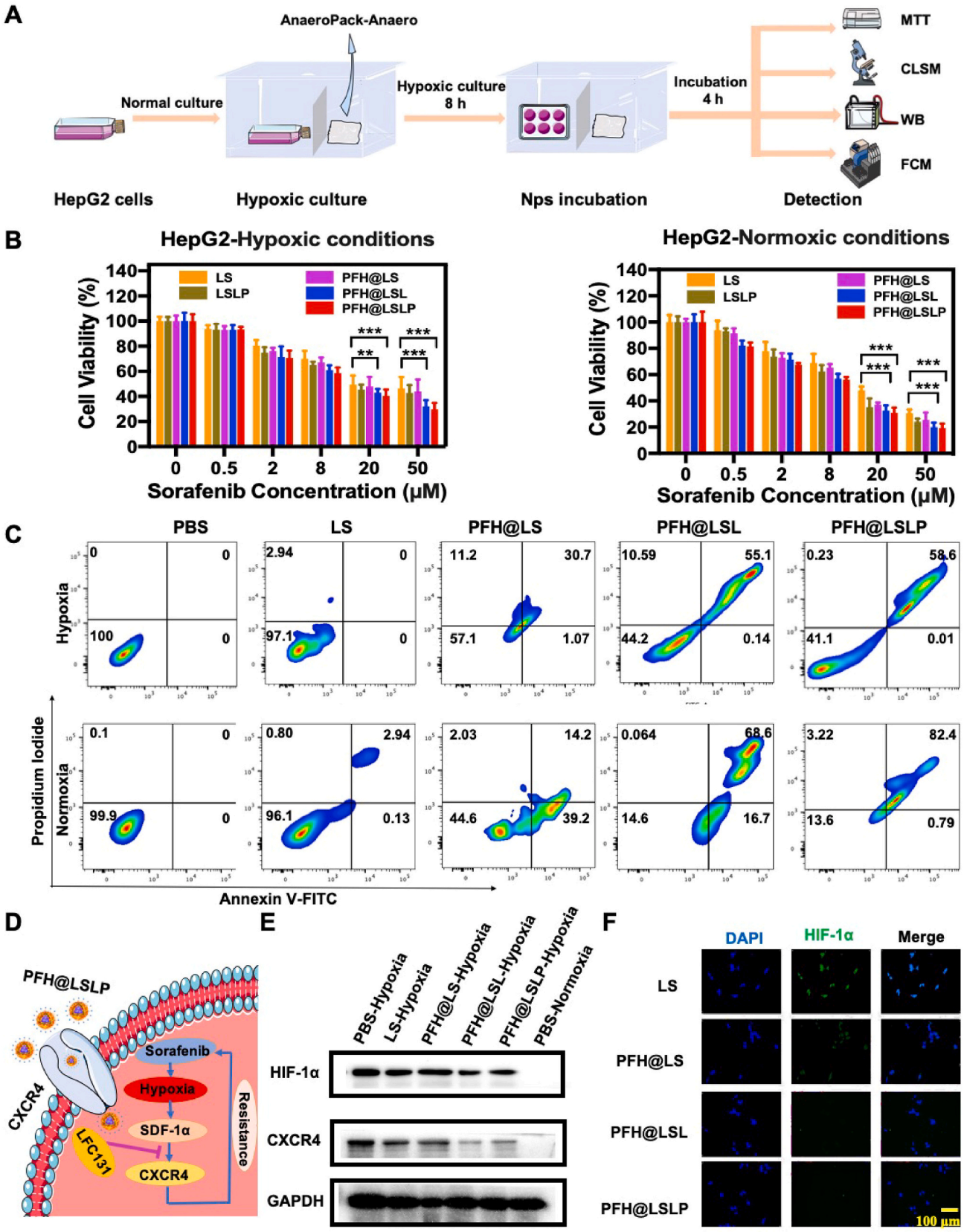

Fig. 2. Cytotoxicity and mechanism of PFH@LSLP under hypoxic conditions. (A) Schematic illustration of HepG2 cells cultured with PFH@LSLP in hypoxic conditions for *in vitro* antitumor evaluation. (B) Cell viability of tumor (HepG2) cells determined by MTT assay under hypoxic conditions and normoxic conditions at 37 °C. (C) Cell apoptosis measured by Annexin V-FITC and PI staining assay in hypoxic and normoxic conditions, respectively. (D) Schematic illustration of PFH@LSLP overcoming resistance to sorafenib through the SDF-1α/CXCR4 pathway under hypoxic conditions. (E) Western blotting assay of HIF-1α and CXCR4 expression modulated by PFH@LSLP under hypoxic conditions. (F) Immunofluorescence analysis of HIF-1α expression of HepG2 cells after incubation with different formulations (PFH@LSLP, PFH@LSL, PFH@LS and LS) in hypoxic conditions for 4 h at 37 °C. Scale bar: 100 μm **$p < 0.01$, ***$p < 0.001$.

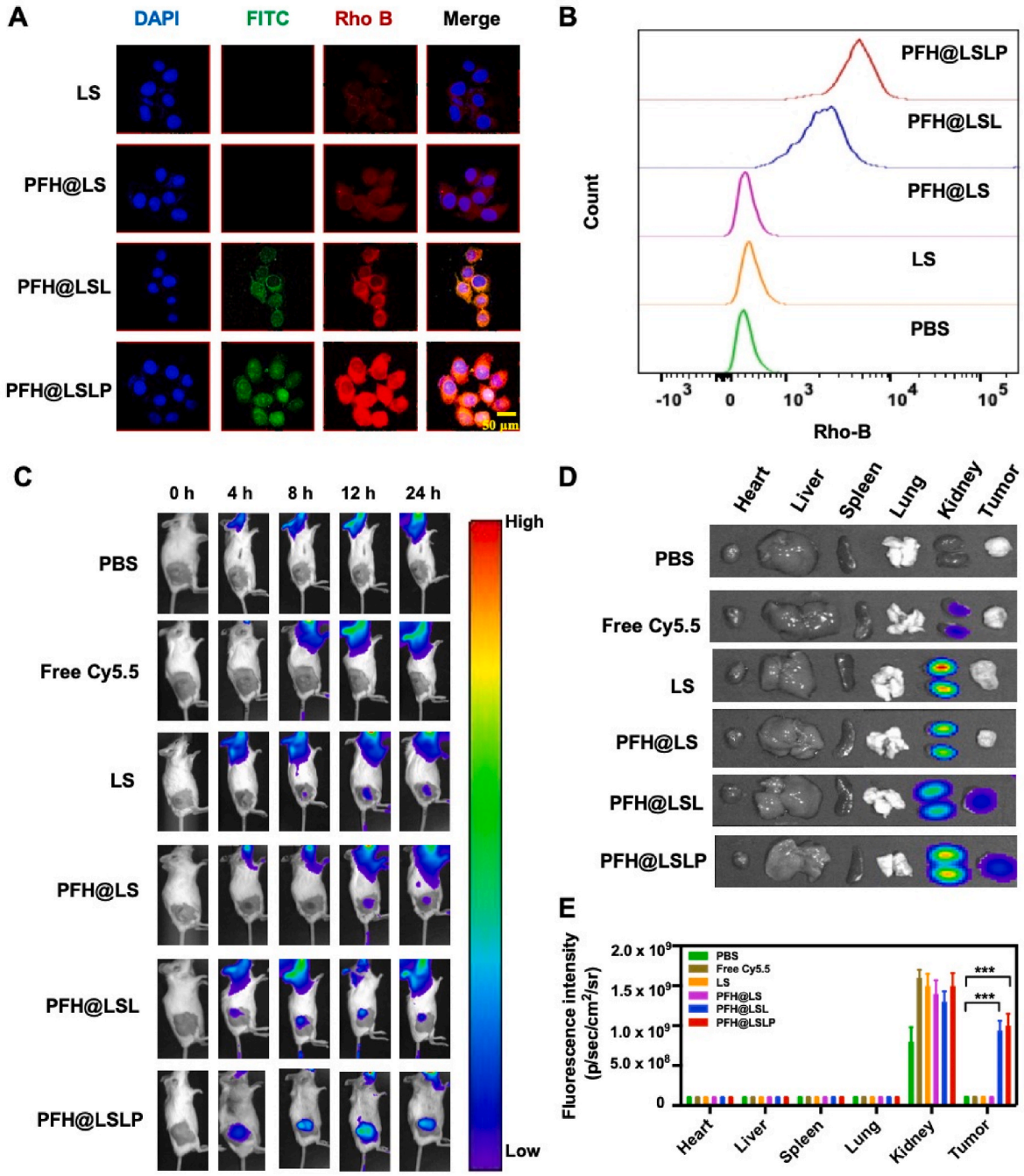

Fig. 3. Cellular uptake and tumor-specific biodistribution of PFH@LSLP nanoparticles. (A) Cellular uptake of PFH@LSLP by HepG2 cells in hypoxic conditions. The specific peptide LFC131 was labeled by FITC and Rho B was encapsulated to mimic drugs. Scale bars: 50 μm. (B) Flow cytometry of the fluorescence intensity of Rho B from PFH@LSLP in hypoxic conditions. (C) *In vivo* fluorescence distribution of H22 tumor-bearing BALB/c mice after *i.v.* injection of various Cy5.5-labeled nanoparticles at different time points. Representative *ex vivo* fluorescent images (D) and corresponding fluorescence intensity (E) of Cy5.5 in tumors and major organs (heart, liver, spleen, lung and kidney) collected from mice 24 h post-administration of Cy5.5-labeled nanoparticles. Data are presented as the mean ± SD (n = 3). ***$p < 0.001$, assessed using Student's *t*-test and one-way ANOVA followed by a post hoc test.

histological and immunohistochemical investigation of tumor tissues harvested from mice after various treatments were stained and submitted for hematoxylin and eosin (H&E), Ki67 and TUNEL observation, respectively (Fig. 4G). The quantitative analysis of Ki67 and TUNEL was provided in Fig. S8. Consistently, the PFH@LSLP treatment performed the most obvious induction of apoptosis and necrosis of HCC cells, much more serious than that of the PFH@LSL or PFH@LS, further confirming that PFH@LSLP could overcome sorafenib-resistance to achieve synergistic antitumor effect by hypoxia remission and immune response activation.

To further verify the biosafety of the liposomes, the major organs (heart, liver, spleen, lung, and kidney) and serum of mice were collected 2 d after the end of liposomal treatments for histological and blood biochemical examination (Figs. S9–S10). No pathological changes were found after treatment with PFH@LSLP or other liposomal nanoparticles. Meanwhile, there were also no abnormality was found in blood physiology and blood biochemical indicators (AST, ALT, BUN, CR, CK, LDH-L, CK-MB) after nanoparticles treatments. Therefore, it is reasonable to believe that PFH@LSLP was a promising potent therapeutic strategy with a good biocompatibility.

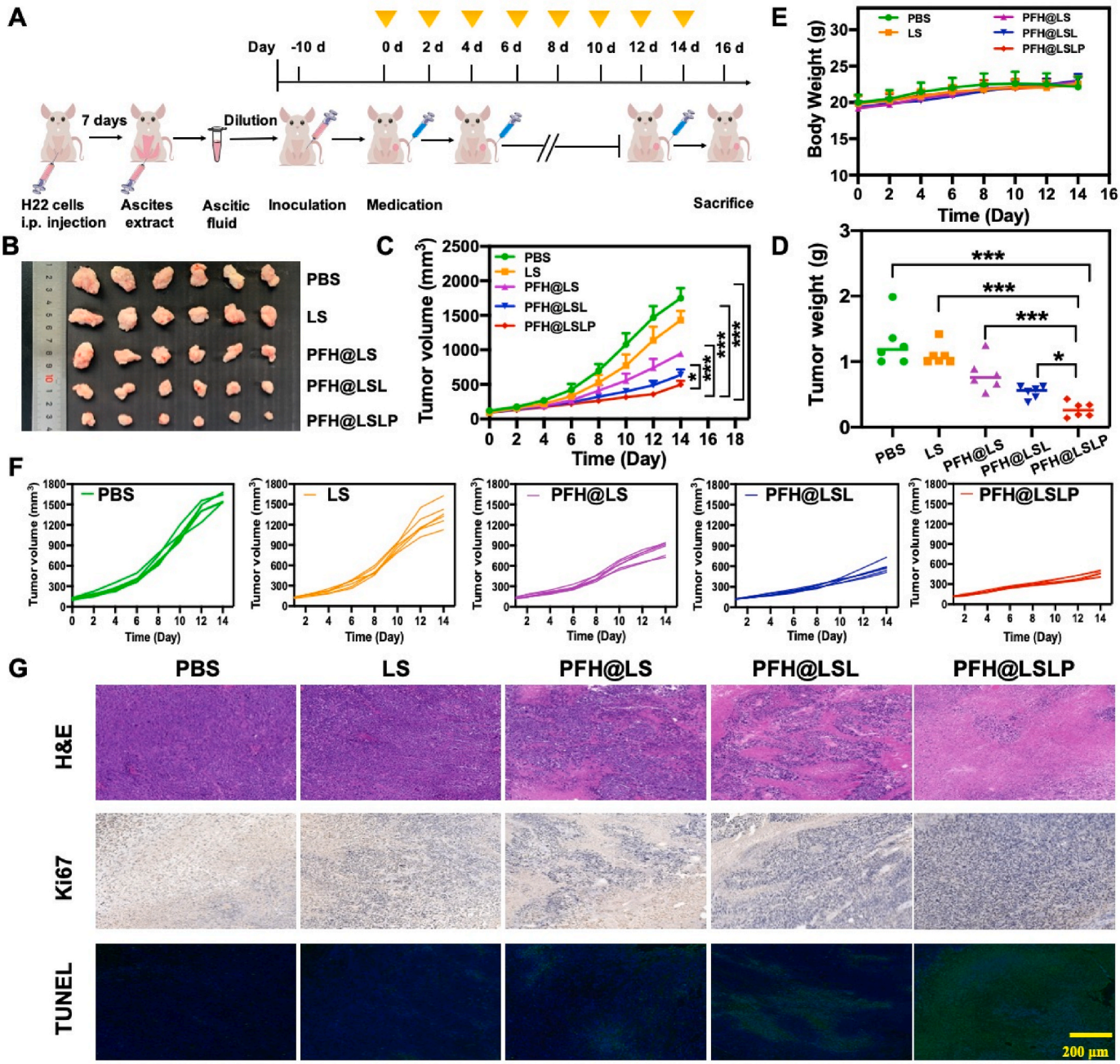

Fig. 4. *In vivo* antitumor effects of PFH@LSLP on H22 tumor-bearing mice. (A) Schematic illustration of the establishment of the H22 mice tumor models and medication process for *in vivo* therapeutic studies. (B) Photographs of tumors collected at the end of antitumor studies (n = 6). (C) Tumor growth curves of mice after *i.v.* injection with different formulations (n = 6). (D) Tumor weights at the end of each treatment (n = 6). (E) Body weights of tumor-bearing mice receiving various treatments (n = 6). (F) Primary tumor growth curves of individual mouse from each group. (G) H&E, Ki67 and TUNEL analyses of H22 tumor tissue sections harvested from mice after receiving various treatments. Scale bar: 200 μm *P < 0.05, **P < 0.01, ***P < 0.001.

2.5. In vivo immune activation by PFH@LSLP

Currently, as an alternative approach to directly target tumor cells, the regulation of TAMs is emerging as a feasible therapeutic strategy for solid tumors [35]. CSF1 is a key regulator of the macrophage differentiation that sustains the pro-tumorigenic functions of TAMs [36]. CSF1 secreted by cancer cells binds to CSF1R on TAM and in turn activates the downstream signaling pathway responsible for the increase in TAM polarization to the immunosuppressive phenotype [37,38]. In that regard, blocking the CSF1/CSF1R pathway has been reported to modulate the immunosuppression status of HCC microenvironment, alter macrophage recruitment and M2 phenotype polarization, which subsequently activated $CD8^+$ T cells and sensitized immune-dependent HCC to sorafenib resistance [39]. In summary, we investigated whether PFH@LSLP could improve the efficacy of ICD and promote the peripheral effect by inhibiting CSF1/CSF1R pathway responsible for the TAM immunosuppressive phenotype, stimulating the production and infiltration of effector T cells by activating DCs.

To further investigate the immune responses activated by PFH@LSLP, the typical cell types of innate immunity (macrophages) and cellular immunity (T cells) were detected, respectively. As illustrated in Fig. 5A, the proportion of $CD8^+$ T cells ($CD3^+$ $CD8^+$) in tumor tissues determined by FCM was appreciably increased to 13.1% in PFH@LSLP group, which was much higher than the PBS, LS, PFH@LS, and

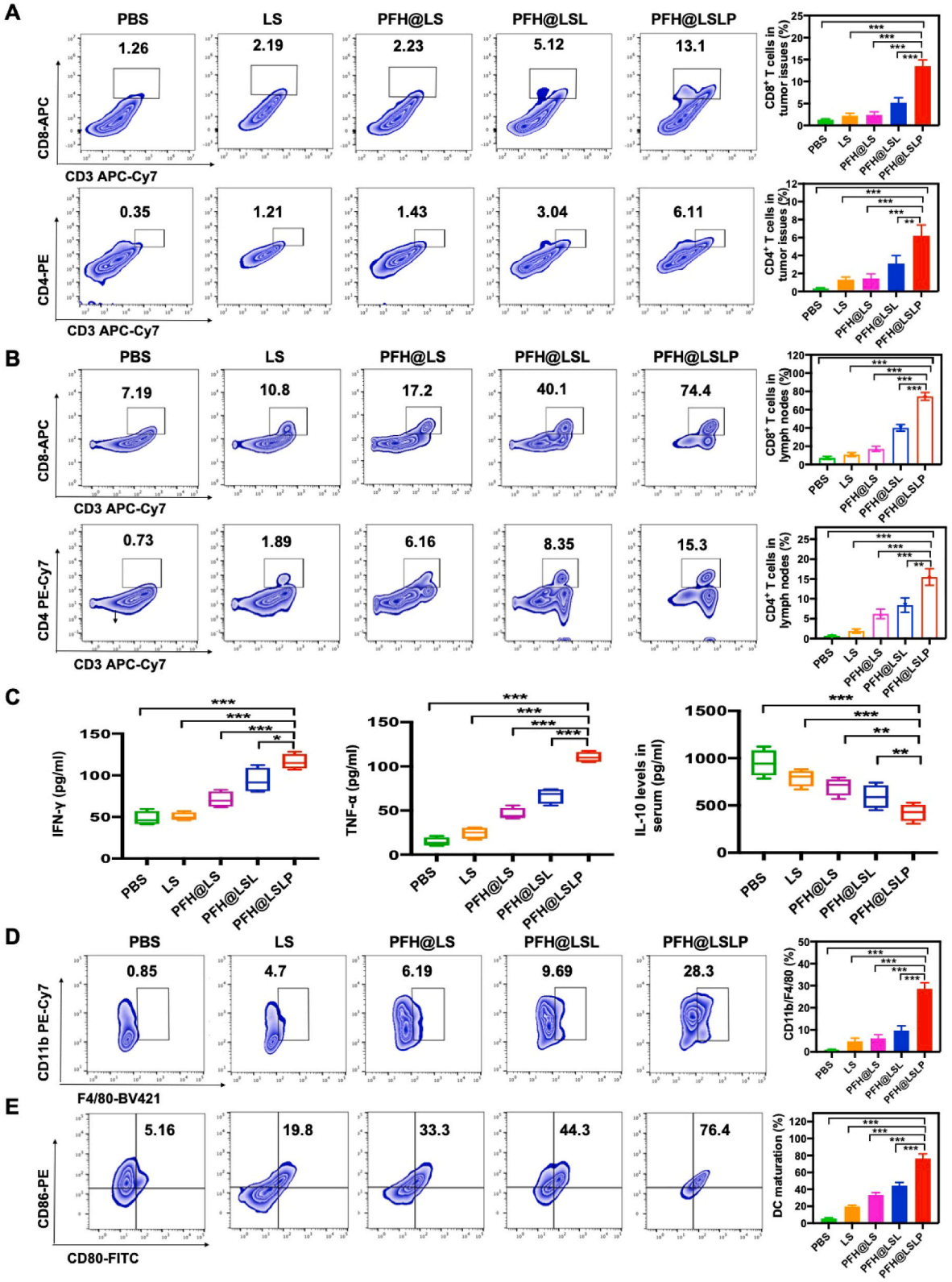

Fig. 5. *In vivo* immune activation by PFH@LSLP on H22 tumor-bearing mice. FCM quantification of infiltration of $CD8^+$ and $CD4^+$ T cells (gated on $CD3^+$ T cells) in tumor tissues (A) and lymph nodes (B). (C) Secretion of interferon-γ (IFN-γ), tumor necrosis factor-α (TNF-α) and interleukin-10 (IL-10) in plasma 16 d after treatments. *$P < 0.05$, **$P < 0.01$, ***$P < 0.001$. (D) FCM quantification of TAMs ($CD11b^+$ $F4/80^+$) frequencies in tumors 16 d after treatments. (E) Quantitative analysis of DCs maturation (gated on $CD11c^+$ $CD80^+$ $CD86^+$) in Lymph node after different treatments.

PFH@LSL groups. Similarly, the infiltration of T helper cells ($CD3^+$ $CD4^+$) was found to reach 6.11% in PFH@LSLP group, which was over 2-fold that of PFH@LSL and about 4-fold that of PFH@LS, respectively.

The more significant upregulating effect of $CD8^+$ and $CD4^+$ T cells infiltration in PFH@LSLP group was found in lymph nodes due to the T cell population was even larger than in tumor tissues (Fig. 5B). Meanwhile, the quantitative statistical analysis of $CD8^+$ T cells and $CD4^+$ T cells in tumor cells and lymph nodes was provided in Fig. 5A and B. Activated $CD8^+$ T cells can also indirectly kill target cells by releasing cytokines such as IFN- γ and TNF-α. Besides, the typical cytokines, interferon-γ (IFN-γ), tumor necrosis factor-α (TNF-α), and interleukin-10 (IL-10), which were the key biomarkers of altered T cells responses released by immune cells of TME were detected by ELISA assay (Fig. 5C). Benefiting from PLX3397, the PFH@LSLP was able to induce immunocytes to secrete IFN-γ and TNF-α as well as decrease IL-10 levels in plasma for immune responses activation. Importantly, the PFH@LS and PFH@LSL also showed obvious improvement of cytokines for tumor-suppressive performance, which confirmed the roles of hypoxic microenvironment normalization by PFH and LFC131 on induction of antitumor immunity. The results demonstrated that the PFH@LSLP group could effectively enhance the activation and infiltration of $CD8^+$ and $CD4^+$ T cells in tumors to perform synergistic immunotherapy.

F4/80 and CD11b biomarkers were then chosen for TAMs infiltration analysis. As shown in Fig. 5D, all of the groups have increased the TAMs ($F4/CD80^+$ and $CD11b^+$) proportion to some extent while PFH@LSLP showed the most significant improvement from 0.85% (PBS group) to 28.3% through FCM and quantitative analysis. Our results demonstrate that PFH@LSLP-mediated CSF1/CSF1R blockade delayed tumor growth by shifting the polarization rather than the depletion of TAMs. Specifically, a significant increase of M1 as well as decrease trend of M2 among TAMs was detected in PFH@LSLP group (Figs. S11 and S12). This result probably ascribed to the great potential of the CSF1/CSF1R inhibitor PLX3397 in PFH@LSLP on polarizing TAMs for reshaping the tumor immune-microenvironment.

The matured DCs would present antigens to T cells and activate adaptive immune responses. Hence, we have evaluated the roles of the liposomes on DCs maturation in lymph nodes. As shown in Fig. 5E, the results of FCM and quantitative analysis showed that the proportion of matured DCs ($CD80^+$ $CD86^+$, gated by $CD11c^+$) was only 5.16% of PBS group, and this number was dramatically increased to 76.4% after PFH@LSLP treatment. However, the other groups only showed limited DCs maturation effect compared to PFH@LSLP. This might be explained by that PFH@LS and PFH@LSL activated tumor immunity was mainly because of hypoxic microenvironment reversion by oxygen diffusion, while PFH@LSLP performed additional immune activation due to presence of PLX3397 acted as an immune adjuvant by blocking the CSF1/CSF1R signaling pathway to promote DCs maturation and T cell activation. Furthermore, the negatively regulated tumor-regulated T cells (Tregs) and MDSCs in tumor immunity were also evaluated in Fig. S13. The $CD4^+$ $Foxp3^+$ (gated by $CD25^+$) cell ratio was significantly reduced after PFH@LSLP treatment. Together, PFH@LSLP could effectively activate the antitumor immunity, which was referred to be caused by hypoxia-related indexes inhibition and CSF1/CSF1R pathway blockage to overcome sorafenib-resistance for combined antitumor therapy.

2.6. Transcriptional evaluation of H22-bearing mice tumor by RNA-sequencing

To further explore the underlying biological mechanism of synergistic tumor therapy of LFC131 peptide and PLX3397 inhibitor in PFH@LSLP NPs, we performed whole genome RNA expression sequencing (RNAseq) on H22-bearing mice exposed to various treatments. By RNA sequencing, tumor gene expression profiles of LS, PFH@LS, PFH@LSL, and PFH@LSLP groups were revealed and were compared with PBS group, which was considered as control. Following with bioinformatic analysis, consistency analysis indicated a high consistency in gene expression of each group, except for a distinct difference shown in PFH@LSLP, which was deduced to be caused by the immune activation of PLX3397 presented in PFH@LSLP under hypoxic conditions (Fig. 6A).

The gene expression relationship between each group was exhibited by the VENN graph (Fig. 6B). Among the 14,975 examined genes, there were 76, 90, 104, and 218 gene transcripts uniquely upregulated in H22-bearing mice treated by LS, PFH@LS, PFH@LSL and PFH@LSLP, respectively. The most genes that exclusively expressed in PFH@LSLP were attributed to the cooperation of LFC131 and PLX 3397, which resulted to the regulation of SDF-1α/CXCR4 and CSF1/CSF1R axis, respectively. For ensuring differential expression level in response to different treatments, Deseq2 was utilized to calculate the relative transcript level compared to the PBS group. The hierarchical clustering of these altered expression gene sets was revealed with absolute log2 fold-change ≥ 1 and p-value < 0.05 as a filter in Fig. S14. As shown in the volcano plots (Fig. 6C), there were 174 genes were upregulated while 123 genes were downregulated in PFH@LSLP group, which were much more significant of gene expression than that of LS (14 genes and 106 genes), PFH@LS (21 genes and 55 genes), and PFH@LSL (59 genes and 10 genes). Furthermore, relative pathways were analyzed with the 'biological process' in the Kyoto Encyclopedia of Genes and Genomes (KEGG) and supervised Gene Ontology (GO) database. Based on Fig. 6D, multiple signaling pathways were significantly affected, e.g., signal transduction, inflammatory response, cell differentiation, and apoptotic process. Compare to the control group LS, a solely drug-mediated approach mainly influenced the signal transduction and apoptosis process, the result of which only led to a limited antitumor effect. In consideration of the significance of hypoxia in tumor microenvironment, the PFH-containing groups (PFH@LS, PFH@LSL, and PFH@LSLP) showed dramatic changes of genes in hypoxia pathway. The results further showed the LFC131-mediated tumor targeting in PFH@LSL and PFH@LSLP contributed to better therapeutic effects by regulating cell adhesion and apoptotic process pathways. Moreover, PFH@LSLP could activate immune responses by the CSF1/CSF1R inhibitor to achieve the most distinct antitumor effect than other groups.

Furthermore, relative treatment approaches were demonstrated in molecular level and more key pathways in PFH@LSLP group from drug, hypoxia suppression, targeting tumor cells and immune activation by identifying the related typical genes (Fig. 6E). PFH@LSLP treatment significantly upregulated the apoptosis-related genes in tumor cells, including IL24, PTN, HMGA2, GADD45A, PHLDA1, JUN, PPP1R15A and RHOB, implied a significant direct therapeutic effect on tumor. Additionally, the expression of relative hypoxia genes in the PFH@LSLP group including DDAH1, CHRNB2, ANGPTL4, UCP3, ADORA1, ADIPOQ and TRPV1 were downregulated, indicating the remission of PFH@LSLP on hypoxia. Meanwhile, the expression of different types of immune cell-expressed genes in the PFH@LSLP group including EREG, IFIT1, RSAD2, CCRL2, THBS1, IRF7, CLCF1, HAVCR2 and PMP22 was also upregulated, suggesting that the PFH@LSLP may stimulate the immune system of H22 cells and recruit immune cells into the tumor microenvironment. All in all, PFH@LSLP treatment integrated drug-based cytotoxicity with hypoxic suppression, and immune activation to construct a comprehensive and highly efficient therapeutic system for tumor therapy.

2.7. In vivo antitumor efficacy of PFH@LSLP on PDX HCC model

Inspired by the synergistic antitumor effect of sorafenib and PLX3397 on H22 tumor-bearing model, the antitumor efficacy of the liposomal nanoparticles was further investigated on the patient-derived tumor xenograft (PDX) model of hepatocellular carcinoma of BALB/c nude mice. As shown in Fig. 7A, HCC PDX model mice were intravenously given 200 μL of PBS, LS, PFH@LS, PFH@LSL, and PFH@LSLP once every two days, respectively. The antitumor performances were shown in Fig. 7B–F, LS showed limited tumor inhibition effect due to the

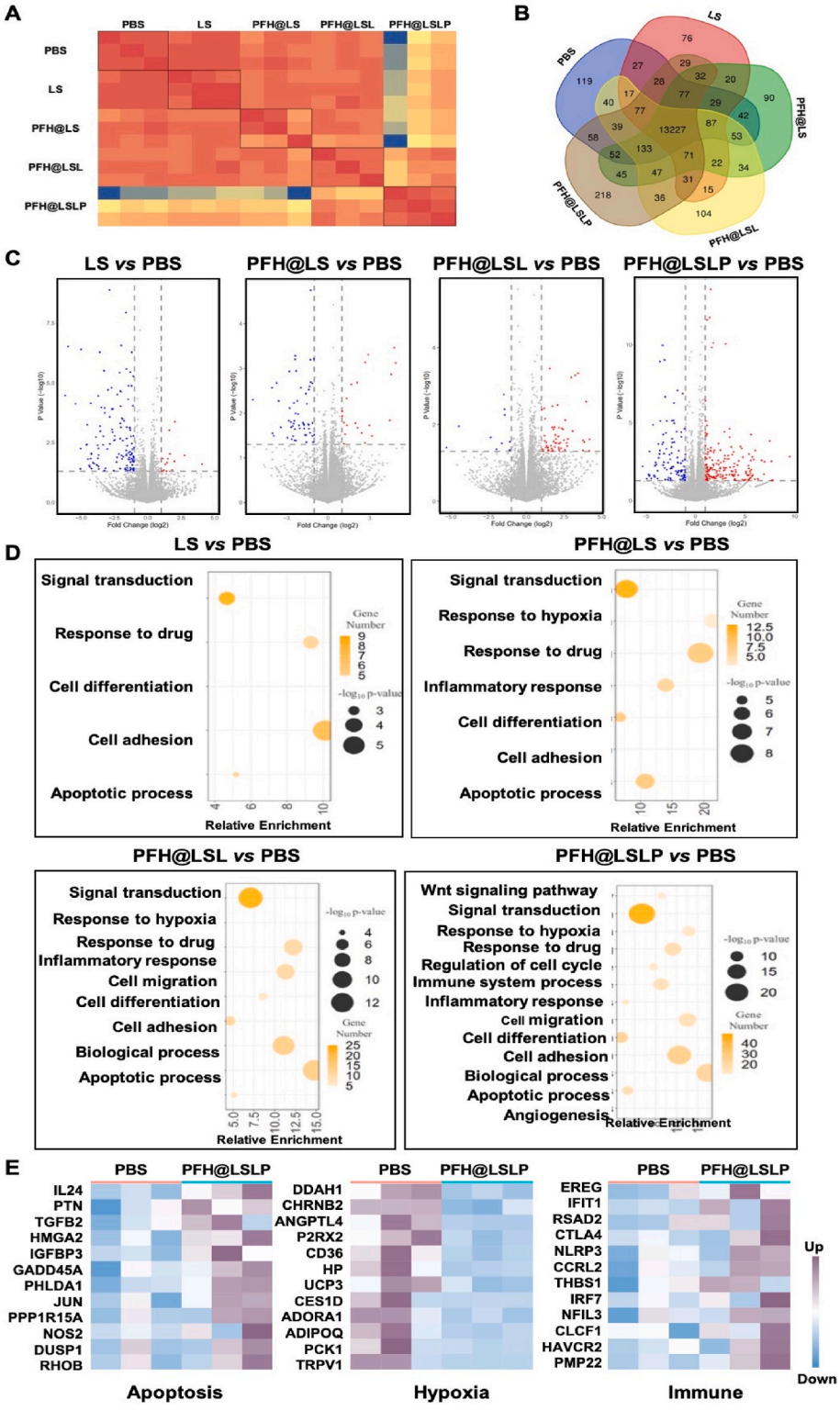

Fig. 6. Transcriptional level of H22-bearing mice tumor in differential treatments by RNA-sequencing. (A) The consistency analysis of 5 groups, including PBS, LS, PFH@LS, PFH@LSL and PFH@LSLP group. (B) The intersection of expressed gene numbers in 5 groups by VENN graph. (C) The volcano plots of differentially expressed genes in LS, PFH@LS, PFH@LSL and PFH@LSLP, compared with PBS group. (D) The GO analysis of differential gene expression between different treatment groups. (E) A heat map of apoptosis, hypoxia and immune related gene expression level in PBS and PFH@LSLP.

deterioration of hypoxia accompanied with sorafenib treatment. On the other hand, the tumor growth was moderately suppressed in the PFH@LS treated group, probably attributed to the hypoxia relief by PFH. Notably, the tumors growth was significantly suppressed in the PFH@LSLP and PFH@LSL treated mice, which displayed potent hypoxia reversion effect not only *via* oxygen delivery but also through the blocking of CXCR4 and its downstream hypoxia-related pathways. The increasing trend of the tumor growth curve of various liposomes was also consistent with the above results. It is noteworthy that PFH@LSL and PFH@LSLP showed inappreciable difference in tumor inhibition, confirming that the sorafenib resistance could be efficiently overcome by hypoxia relief on HCC PDX model. Meanwhile, only small fluctuations of body weight in various groups were observed (Fig. 7E), suggesting PFH@LSLP and PFH@LSL have good biocompatibility and safety, which is consistent with the above results.

In order to illustrate the mechanism how the PFH@LSLP improve

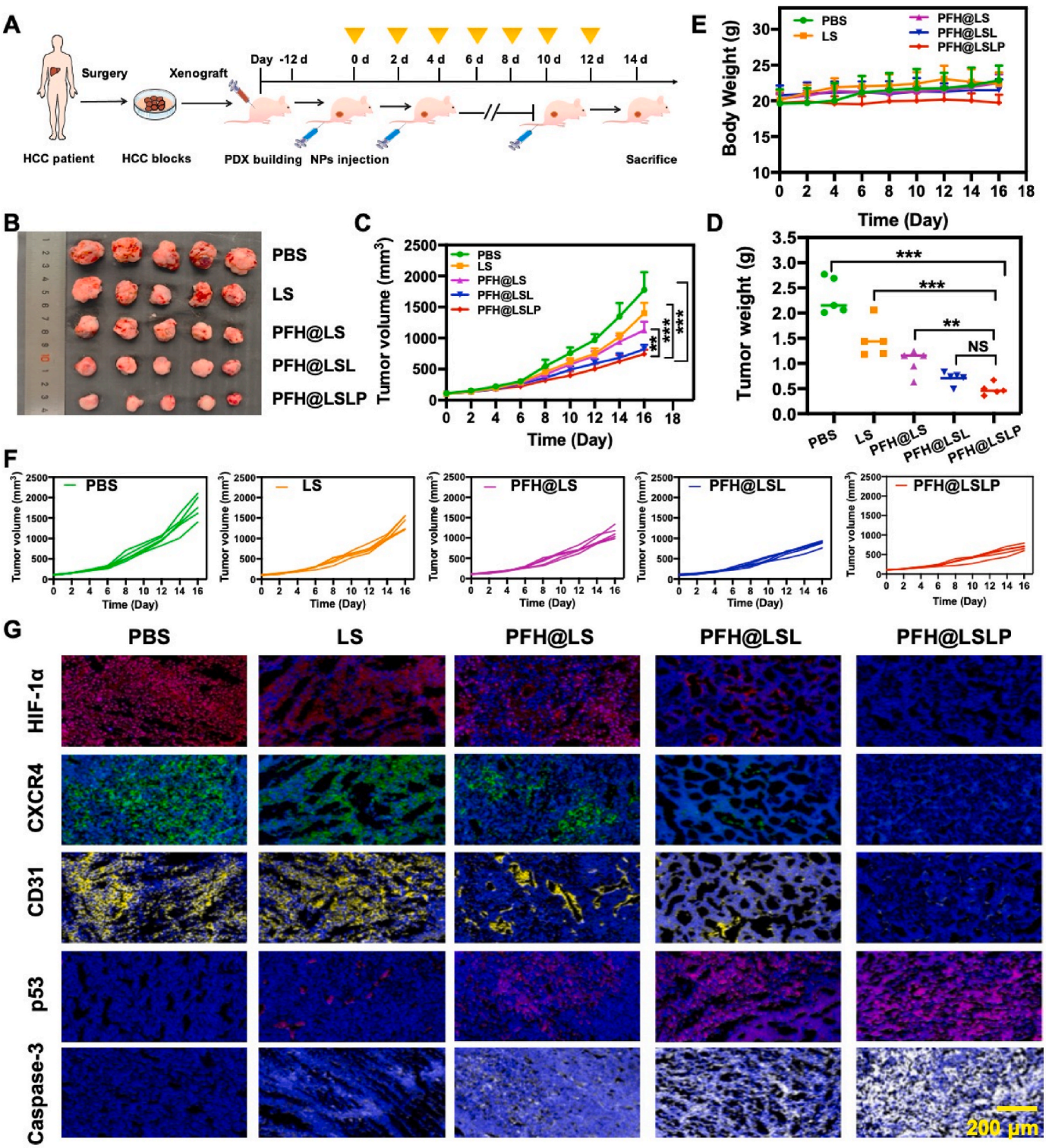

Fig. 7. *In vivo* antitumor effects of PFH@LSLP on HCC PDX mice model. (A) Schematic illustration of the establishment of the HCC PDX model and medication process on BABL/c nude mice. (B) Digital images of tumor tissues after different treatments (n = 5). (C) Tumor growth curves of mice during therapeutic process (n = 5). (D) Tumor weights of excised tumors from mice at 14 d post treatments. (E) Body weight variation of mice receiving different treatments for 14 d. (F) Primary tumor growth curves of individual mouse from each group of HCC PDX mice model (n = 5). (G) Immunofluorescence detection of tumor sections for expression of hypoxic markers (HIF-1α and CXCR4) and apoptotic markers (CD31, p53, caspase 3) after treatments. Scale bar: 200 μm *P < 0.05, **P < 0.01, ***P < 0.001.

antitumor effect by hypoxia regulation, the immunofluorescence staining of tumor sections for hypoxic and inflammatory markers was investigated after treatments (Fig. 7G). The results manifested that the hypoxic areas and the induced HIF-1α and CXCR4 expression in PDX HCC tumors was significantly reduced by PFH@LSL and PFH@LSLP. In contrast, the larger hypoxic areas were still detected in the tumor sections without hypoxia reversion or only with oxygen supply by PFH. Therefore, the vascular marker CD31 was used to assess the extent of angiogenesis (sorafenib is an anti-vascular drug) and tumor growth rate [40]. On the other aspect, P53 is an important tumor suppressor that

regulates multiple cell-intrinsic programs, including cell-cycle arrest and apoptosis, to inhibit tumor growth [41,42]. In addition, CD31, p53 and the cleaved caspase 3 level was significantly upregulated under synergistic functions of PFH and LFC131 in PFH@LSL and PFH@LSLP groups, evidencing that the increase of oxidation level would further induce proinflammatory condition of tumors, causing improved tumor cell apoptosis.

3. Conclusion

In summary, a tumor-specific liposome PFH@LSLP with hypoxia normalization and immune activation functions was constructed for sorafenib-resistant tumor therapy. Firstly, PFH was encapsulated in liposomes as an O_2 reservoir to relief tumor hypoxia. Secondly, LFC131 peptide was decorated on the liposomal surface to endow them tumor targeting capability, which would recognize and bind to the CXCR4 overexpressed on HCC cells, and then blocked the downstream SDF-1α/CXCR4 pathway to overcome hypoxia-related sorafenib resistance. Furthermore, the combined application of CSF1/CSF1R inhibitor PLX3397 would further activate tumor immunity via increasing infiltration of $CD8^+$ T cells and matured DC cells in the tumors and lymph nodes, meanwhile remodeling the tumorigenic immune microenvironment to tumor-suppressive conditions. Therefore, the multifunctional TME regulation strategy for synergistic chemo-immunotherapy greatly improved the therapeutic effect of sorafenib resistant tumors.

Funding sources

Any funds used to support the research of the manuscript should be placed here (per journal style).

Notes

Any additional relevant notes should be placed here.

CRediT authorship contribution statement

Yuehua Wang: Conceptualization, Methodology, Formal analysis, Writing – original draft. **ZhenJie Wang:** Investigation, Data curation. **Fei Jia:** Methodology, Software. **Qing Xu:** Investigation, Resources. **Zhilin Shu:** Investigation, Resources. **Junlin Deng:** Investigation, Resources. **Aimin Li:** Supervision. **Meng Yu:** Supervision, Writing – review & editing, Project administration. **Zhiqiang Yu:** Supervision, Funding acquisition.

Declaration of competing interest

The authors declare that they have no known competing financial interests or personal relationships that could have appeared to influence the work reported in this paper.

Acknowledgements

This research was financially supported by GDNRC [Guangdong nature resource center] (2020) 037, the National Natural Science Foundation of China (81773642, 52073139), the Natural Science Foundation of Guangdong Province (2019A1515011619 and 2019A1515011498), and Key Laboratory of Biomedical Effects of Nanomaterials and Nanosafety, National Center for Nanoscience and Technology, CAS (NSKF201819), Project of Traditional Chinese Medicine Bureau of Guangdong Province, China (NO.20203006) and Science and Technology Program of Guangzhou, China (NO.202002030075). Patient hepatocellular carcinoma specimens were obtained according to the guidelines approved by ICE for Clinical Research and Animal Trials of the First Affiliated Hospital of Sun Yat-sen University Approval Letter for Research Protocol (2019151), with the informed consent from the patients.

Appendix A. Supplementary data

Supplementary data to this article can be found online at https://doi.org/10.1016/j.bioactmat.2022.01.003.

References

[1] J. Candia, E. Bayarsaikhan, M. Tandon, A. Budhu, M. Forgues, L.O. Tovuu, U. Tudev, J. Lack, A. Chao, J. Chinburen, X.W. Wang, The genomic landscape of Mongolian hepatocellular carcinoma, Nat. Commun. 11 (2020) 4383.
[2] Y. Xia, G. Tang, Y. Chen, C. Wang, M. Guo, T. Xu, M. Zhao, Y. Zhou, Tumor-targeted delivery of siRNA to silence Sox2 gene expression enhances therapeutic response in hepatocellular carcinoma, Bioactive Materials 6 (2021) 1330–1340.
[3] J. Bruix, G.J. Gores, V. Mazzaferro, Hepatocellular carcinoma: clinical frontiers and perspectives, Gut 63 (2014) 844–855.
[4] M. Maluccio, A. Covey, Recent progress in understanding, diagnosing, and treating hepatocellular carcinoma, CA Cancer J Clin 62 (2012) 394–399.
[5] Y. Wang, W. Shang, H. Zhong, T. Luo, M. Niu, K. Xu, J. Tian, Tumor vessel targeted self-assemble nanoparticles for amplification and prediction of the embolization effect in hepatocellular carcinoma, ACS Nano 14 (2020) 14907–14918.
[6] J. Xu, J. Liang, Y.M. Meng, J. Yan, X.J. Yu, C.Q. Liu, L. Xu, S.M. Zhuang, L. Zheng, Vascular CXCR4 expression promotes vessel sprouting and sensitivity to sorafenib treatment in hepatocellular carcinoma, Clin. Cancer Res. 23 (2017) 4482–4492.
[7] M. Ringelhan, D. Pfister, T. O'Connor, E. Pikarsky, M. Heikenwalder, The immunology of hepatocellular carcinoma, Nat. Immunol. 19 (2018) 222–232.
[8] J.L. Raoul, M. Kudo, R.S. Finn, J. Edeline, M. Reig, P.R. Galle, Systemic therapy for intermediate and advanced hepatocellular carcinoma: sorafenib and beyond, Cancer Treat Rev. 68 (2018) 16–24.
[9] J. Chen, R. Jin, J. Zhao, J. Liu, H. Ying, H. Yan, S. Zhou, Y. Liang, D. Huang, X. Liang, H. Yu, H. Lin, X. Cai, Potential molecular, cellular and microenvironmental mechanism of sorafenib resistance in hepatocellular carcinoma, Cancer Lett. 367 (2015) 1–11.
[10] Y. Liang, T. Zheng, R. Song, J. Wang, D. Yin, L. Wang, H. Liu, L. Tian, X. Fang, X. Meng, H. Jiang, J. Liu, L. Liu, Hypoxia-mediated sorafenib resistance can be overcome by EF24 through Von Hippel-Lindau tumor suppressor-dependent HIF-1α inhibition in hepatocellular carcinoma, Hepatology 57 (2013) 1847–1857.
[11] T. Zhou, X. Liang, P. Wang, Y. Hu, Y. Qi, Y. Jin, Y. Du, C. Fang, J. Tian, A hepatocellular carcinoma targeting nanostrategy with hypoxia-ameliorating and photothermal abilities that, combined with immunotherapy, inhibits metastasis and recurrence, ACS Nano 14 (2020) 12679–12696.
[12] S. Ling, Q. Shan, Q. Zhan, Q. Ye, P. Liu, S. Xu, X. He, J. Ma, J. Xiang, G. Jiang, X. Wen, Z. Feng, Y. Wu, T. Feng, L. Xu, K. Chen, X. Zhang, R. Wei, C. Zhang, B. Cen, H. Xie, P. Song, J. Liu, S. Zheng, X. Xu, USP22 promotes hypoxia-induced hepatocellular carcinoma stemness by a HIF1α/USP22 positive feedback loop upon TP53 inactivation, Gut 69 (2020) 1322–1334.
[13] J. Zhuang, M. Ying, K. Spiekermann, M. Holay, Y. Zhang, F. Chen, H. Gong, J. H. Lee, W. Gao, R.H. Fang, L. Zhang, Biomimetic nanoemulsions for oxygen delivery in vivo, Adv Mater 30 (2018), e1804693.
[14] J.L. Markman, A. Rekechenetskiy, E. Holler, J.Y. Ljubimova, Nanomedicine therapeutic approaches to overcome cancer drug resistance, Adv. Drug Deliv. Rev. 65 (2013) 1866–1879.
[15] X. Song, L. Feng, C. Liang, K. Yang, Z. Liu, Ultrasound triggered tumor oxygenation with oxygen-shuttle nanoperfluorocarbon to overcome hypoxia-associated resistance in cancer therapies, Nano Lett. 16 (2016) 6145–6153.
[16] F. Zhang, J. Zhuang, B. Esteban Fernández de Ávila, S. Tang, Q. Zhang, R.H. Fang, L. Zhang, J. Wang, A nanomotor-based active delivery system for intracellular oxygen transport, ACS Nano 13 (2019) 11996–12005.
[17] D.G. Duda, S.V. Kozin, N.D. Kirkpatrick, L. Xu, D. Fukumura, R.K. Jain, CXCL12 (SDF1alpha)-CXCR4/CXCR7 pathway inhibition: an emerging sensitizer for anticancer therapies, Clin. Cancer Res. 17 (2011) 2074–2080.
[18] Y. Chen, Y. Huang, T. Reiberger, A.M. Duyverman, P. Huang, R. Samuel, L. Hiddingh, S. Roberge, C. Koppel, G.Y. Lauwers, A.X. Zhu, R.K. Jain, D.G. Duda, Differential effects of sorafenib on liver versus tumor fibrosis mediated by stromal-derived factor 1 alpha/C-X-C receptor type 4 axis and myeloid differentiation antigen-positive myeloid cell infiltration in mice, Hepatology 59 (2014) 1435–1447.
[19] Y. Hu, X. Li, Q. Zhang, Z. Gu, Y. Luo, J. Guo, X. Wang, Y. Jing, X. Chen, J. Su, Exosome-guided bone targeted delivery of Antagomir-188 as an anabolic therapy for bone loss, Bioactive Materials 6 (2021) 2905–2913.
[20] C. Chittasupho, K. Lirdprapamongkol, P. Kewsuwan, N. Sarisuta, Targeted delivery of doxorubicin to A549 lung cancer cells by CXCR4 antagonist conjugated PLGA nanoparticles, Eur. J. Pharm. Biopharm. 88 (2014) 529–538.
[21] N. Zheng, W. Liu, B. Li, H. Nie, J. Liu, Y. Cheng, J. Wang, H. Dong, L. Jia, Co-delivery of sorafenib and metapristone encapsulated by CXCR4-targeted PLGA-PEG nanoparticles overcomes hepatocellular carcinoma resistance to sorafenib, J. Exp. Clin. Cancer Res. 38 (2019) 232.
[22] S. Xu, S. Ling, Q. Shan, Q. Ye, Q. Zhan, G. Jiang, J. Zhuo, B. Pan, X. Wen, T. Feng, H. Lu, X. Wei, H. Xie, S. Zheng, J. Xiang, Y. Shen, X. Xu, Self-activated cascade-responsive sorafenib and USP22 shRNA Co-delivery system for synergetic hepatocellular carcinoma therapy, Adv. Sci. 8 (2021), 2003042.

[23] W.B. Zhu, Z.F. Zhao, X. Zhou, AMD3100 inhibits epithelial-mesenchymal transition, cell invasion, and metastasis in the liver and the lung through blocking the SDF-1α/CXCR4 signaling pathway in prostate cancer, J. Cell. Physiol. 234 (2019) 11746–11759.
[24] X. Sun, Z. Cao, K. Mao, C. Wu, H. Chen, J. Wang, X. Wang, X. Cong, Y. Li, X. Meng, X. Yang, Y.G. Yang, T. Sun, Photodynamic therapy produces enhanced efficacy of antitumor immunotherapy by simultaneously inducing intratumoral release of sorafenib, Biomaterials 240 (2020), 119845.
[25] M. Yang, J. Li, P. Gu, X. Fan, The application of nanoparticles in cancer immunotherapy: targeting tumor microenvironment, Bioactive Materials 6 (2021) 1973–1987.
[26] S.R. Gordon, R.L. Maute, B.W. Dulken, G. Hutter, B.M. George, M.N. McCracken, R. Gupta, J.M. Tsai, R. Sinha, D. Corey, A.M. Ring, A.J. Connolly, I.L. Weissman, PD-1 expression by tumour-associated macrophages inhibits phagocytosis and tumour immunity, Nature 545 (2017) 495–499.
[27] J. Zhao, L. Dong, B. Lu, G. Wu, D. Xu, J. Chen, K. Li, X. Tong, J. Dai, S. Yao, M. Wu, Y. Guo, Down-regulation of osteopontin suppresses growth and metastasis of hepatocellular carcinoma via induction of apoptosis, Gastroenterology 135 (2008) 956–968.
[28] B.S. Sun, Q.Z. Dong, Q.H. Ye, H.J. Sun, H.L. Jia, X.Q. Zhu, D.Y. Liu, J. Chen, Q. Xue, H.J. Zhou, N. Ren, L.X. Qin, Lentiviral-mediated miRNA against osteopontin suppresses tumor growth and metastasis of human hepatocellular carcinoma, Hepatology 48 (2008) 1834–1842.
[29] Y. Zhu, J. Yang, D. Xu, X.M. Gao, Z. Zhang, J.L. Hsu, C.W. Li, S.O. Lim, Y.Y. Sheng, Y. Zhang, J.H. Li, Q. Luo, Y. Zheng, Y. Zhao, L. Lu, H.L. Jia, M.C. Hung, Q.Z. Dong, L.X. Qin, Disruption of tumour-associated macrophage trafficking by the osteopontin-induced colony-stimulating factor-1 signalling sensitises hepatocellular carcinoma to anti-PD-L1 blockade, Gut 68 (2019) 1653–1666.
[30] T. Zhu, H. Wang, Z. Jing, D. Fan, Z. Liu, X. Wang, Y. Tian, High efficacy of tetra-PEG hydrogel sealants for sutureless dural closure, Bioactive Materials 8 (2022) 12–19.
[31] A. Mantovani, S. Sozzani, M. Locati, P. Allavena, A. Sica, Macrophage polarization: tumor-associated macrophages as a paradigm for polarized M2 mononuclear phagocytes, Trends Immunol. 23 (2002) 549–555.
[32] Z.T. Chai, X.D. Zhu, J.Y. Ao, W.Q. Wang, D.M. Gao, J. Kong, N. Zhang, Y.Y. Zhang, B.G. Ye, D.N. Ma, H. Cai, H.C. Sun, microRNA-26a suppresses recruitment of macrophages by down-regulating macrophage colony-stimulating factor expression through the PI3K/Akt pathway in hepatocellular carcinoma, J. Hematol. Oncol. 8 (2015) 56.
[33] S. Sangaletti, C. Tripodo, S. Sandri, I. Torselli, C. Vitali, C. Ratti, L. Botti, A. Burocchi, R. Porcasi, A. Tomirotti, M.P. Colombo, C. Chiodoni, Osteopontin shapes immunosuppression in the metastatic niche, Cancer Res. 74 (2014) 4706–4719.
[34] S. Mok, R.C. Koya, C. Tsui, J. Xu, L. Robert, L. Wu, T. Graeber, B.L. West, G. Bollag, A. Ribas, Inhibition of CSF-1 receptor improves the antitumor efficacy of adoptive cell transfer immunotherapy, Cancer Res. 74 (2014) 153–161.
[35] L. Cassetta, J.W. Pollard, Targeting macrophages: therapeutic approaches in cancer, Nat. Rev. Drug Discov. 17 (2018) 887–904.
[36] M.B. Buechler, W. Fu, S.J. Turley, Fibroblast-macrophage reciprocal interactions in health, fibrosis, and cancer, Immunity 54 (2021) 903–915.
[37] J.A. Joyce, J.W. Pollard, Microenvironmental regulation of metastasis, Nat. Rev. Cancer 9 (2009) 239–252.
[38] D.A. Hume, K.P. MacDonald, Therapeutic applications of macrophage colony-stimulating factor-1 (CSF-1) and antagonists of CSF-1 receptor (CSF-1R) signaling, Blood 119 (2012) 1810–1820.
[39] A. Mantovani, F. Marchesi, A. Malesci, L. Laghi, P. Allavena, Tumour-associated macrophages as treatment targets in oncology, Nat. Rev. Clin. Oncol. 14 (2017) 399–416.
[40] J. Xu, J. Liang, Y.M. Meng, J. Yan, Yu Xj, C.Q. Liu, L. Xu, S.M. Zhuang, L. Zheng, Vascular CXCR4 expression promotes vessel sprouting and sensitivity to sorafenib treatment in hepatocellular carcinoma, Clin. Cancer Res. 23 (2017) 4482–4492.
[41] J. Mu, X. Xie, S.S. Xiong, Y.H. Zhang, Y.T. Wang, Q. Zhao, H.P. Zhu, W. Huang, G. He, Discovery of spirooxindole–ferrocene hybrids as novel MDM2 inhibitors, Chin. Chem. Lett. 32 (2021), 189701901.
[42] N. Raj, L.D. Attardi, Tumor suppression: p53 alters immune surveillance to restrain liver cancer, Curr. Biol. 23 (2013) 527–530.